



Structural and electronic properties of nonconventional α -graphyne nanocarbons

Thainá Araújo Oliveira,¹ Paloma Vieira Silva ,^{2,3} Aldilene Saraiva-Souza,⁴
José Gadelha da Silva Filho,⁵ and Eduardo Costa Girão ^{1,3}

¹Programa de Pós-Graduação em Ciência e Engenharia dos Materiais, Universidade Federal do Piauí, CEP 64049-550, Teresina-PI, Brazil

²Instituto Federal de Educação, Ciência e Tecnologia do Amapá, Campus Porto Grande, CEP 68997-000, Porto Grande, Amapá, Brazil

³Departamento de Física, Universidade Federal do Piauí, 64049-550 Teresina, Piauí, Brazil

⁴Departamento de Física, Universidade Federal do Maranhão, Campus Universitário do Bacanga,
CEP 65080-805, Sao Luís, Maranhão, Brazil

⁵Centro de Ciências Sociais, Saúde e Tecnologia, Universidade Federal do Maranhão, Imperatriz, MA, 65900-410, Brazil



(Received 18 March 2021; revised 14 December 2021; accepted 21 December 2021; published 21 January 2022)

In this work, we propose a set of nonconventional graphyne lattices inspired by previously studied sp^2 nanocarbon sheets, known as haeckelites, and we study their electronic properties by density functional theory methods. Two of these systems are solely composed of five- and seven-membered rings in rectangular lattices, while a third system features a mixture of five-, six-, and seven-polygonal rings in a hexagonal network. We show that these systems exhibit dynamical, thermal, and mechanical stability as demonstrated by phonon band structures, molecular dynamics simulations, and by the computation of their elastic constants. The three lattices exhibit a metallic nature similar to their full- sp^2 counterparts. However, the graphynes' electronic properties are strongly different from those of the original haeckelites, as the largest contribution to their frontier states comes from the sp hybridized atoms. Furthermore, the three proposed systems feature different electronic signatures from each other, as their frontier states feature different energy ranges for forbidden electronic states, and one of them features a set of Dirac-like cones.

DOI: [10.1103/PhysRevMaterials.6.016001](https://doi.org/10.1103/PhysRevMaterials.6.016001)

I. INTRODUCTION

Nanocarbon science is a broad field of research and technology dealing with materials at different dimensionalities, from zero-dimensional (0D) carbon dots (CDs) to three-dimensional (3D) carbon-based structures, with outstanding physical properties [1–5]. In particular, two-dimensional (2D) carbon forms became a central research topic after groundbreaking experiments regarding graphene materials [4,6]. This honeycomb lattice has exceptional mechanical [7], electronic [8,9], and optical [10] properties with a large potential for nanotechnology applications. Such successful preparation of graphene has inspired further experimental and theoretical studies of new 2D carbon allotropes with different lattice structures and physical properties [11–14]. From a theoretical perspective, several nonhexagonal-shaped 2D materials have been proposed via computational calculations [15–18]. While these are mostly sp^2 structures, other hybridization schemes have also been considered, including mixed sp - sp^2 [19] and sp^2 - sp^3 forms [20,21].

Graphynes (GYs) are a relevant example of nanostructures with mixed hybridization configurations. They were theoretically proposed by Baughman *et al.* [22] in 1987, being conceptually constructed by inserting acetylenic bonds (sp hybridization) in between atoms from a graphene lattice. GYs can be classified into several distinct groups depending on the quantity and position of the sp bonds, and according to the atomic arrangements in the unit cell. These include, for in-

stance, the α -GY, β -GY, and γ -GY forms [23,24], which have been widely studied in the literature. We will refer to them hereafter as *conventional* GYs. This family of 2D nanocarbons gained notoriety since the first experimental observation of graphdiyne (GDY), a structure similar to γ -GY containing two-units-long acetylenic chains [25]. On that occasion, a semiconductor GDY film was successfully synthesized over a copper surface through a cross-coupling reaction. Matsuoka *et al.* [12] reported the synthesis of a GDY analog, referred to as TP-GDY, a free-standing layered material (wider than 1 mm and a thickness of 220 nm) that features a triphenylene core as the structural basis. More recently, the bottom-up synthesis of a monolayer structure resembling γ - and α -graphdiyne was accomplished via a surface-assisted route by the choice of specific precursors [26]. From a theoretical point of view, Nulakani and Subramanian [27] have proposed novel carbon polymorphs composed of five-membered rings connected with acetylenic links, named Cp-graphyne, having semimetallic behavior and being energetically more favorable than a graphdiyne monolayer. Other studies evaluated the effects of acetylenic linkages in systems based on tetragonal nanocarbon forms [28,29]. In a recent theoretical work, Serafini *et al.* [30] systematically generated several 2D nanocarbons belonging to the graphdienes family with different sp/sp^2 carbon atom ratios and a broad set of electronic properties.

In a review paper, Ivanovskii [31] discussed the concept of GY 2D planar carbon networks formed by non-C6

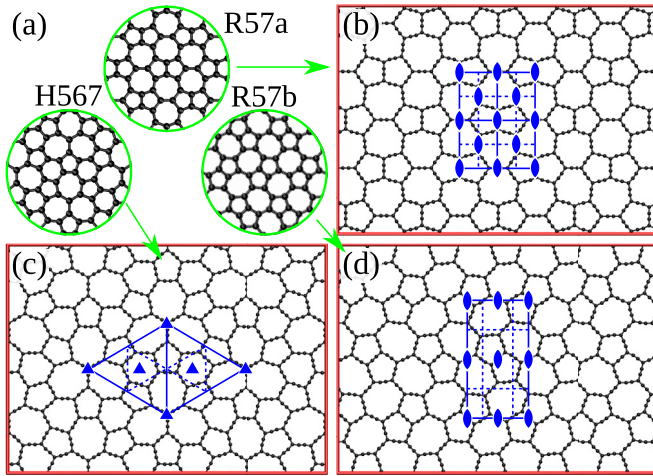


FIG. 1. (a) Atomic structure of the R57a, R57b, and H567 haeckelites. (b)–(d) Atomic structure of the α -R57a, α -H567, and α -R57b systems, respectively, together with a representation of their symmetry groups.

carbon polygons analogous to those in haeckelite structures [15,16,32]. These systems are built by using ordered arrangements of five-, six-, and seven-membered rings in a full- sp^2 carbon network, resulting in rectangular (R57a and R57b) and hexagonal (H567) lattice crystals, which have their structures illustrated in Fig. 1(a). Theoretical calculations have shown that haeckelite systems are intrinsically metallic and more stable than the C60 buckyball [16]. Although these systems have not been synthesized yet, advances on the development of bottom-up synthesis techniques have been successfully used to assemble intricate structures, including hexagonal [33] and nonhexagonal carbon atomic arrangements [34], as well as porous graphene films with random arrangements of polygons [11,35].

When considering the proposal of new hypothetical nanocarbon allotropes, it is relevant to look for a connection with possible strategies for their synthesis/isolation in the laboratory. The construction of nanostructures is pursued, in general, by using either top-down or bottom-up approaches [36]. Top-down approaches are successful in the isolation of graphene out of graphite samples, for instance [4]. However, the lack of macroscopic materials having graphyne structures as their basic units makes bottom-up approaches the most feasible strategy for graphyne synthesis in the near future. In fact, the development and improvement of surface-assisted chemical routes in the past decade allowed the scientific community to create several nanocarbon forms [33,37–42]. These methods are based on tools such as the strategic choices of molecular precursors and specific substrates, as well as temperature conditions. One of the most recent examples is the success in obtaining biphenylene, a planar 2D nanocarbon with four-, six-, and eight-membered rings, that was accomplished by a two-step sequence including linear polymerization of particular monomers followed by interchain HF-zipping reactions [43]. Other examples consist of nanoribbons with nonhexagonal rings prepared experimentally through a surface-assisted chemical route involving dehydrogenative C-C coupling of 2,6-polyazulene

chains [34]. Moving to an example in the graphyne family, a triphenylene-based GDY structure was obtained with a combination of strategically chosen precursors [12]. Considering this scientific context, we believe that realization of several graphynelike structures can be accomplished in the near future by using such approaches.

Motivated by this scenario, we use first-principles calculations to investigate the dynamical stability and electronic properties of three nonconventional (NC) GY structures based on the haeckelite geometries. These are conceptually obtained by the insertion of minimal acetylenic groups between each pair of connected sp^2 atoms in the parent haeckelite sheet. This construction is analogous to the way C = C bonds are replaced in a graphene sheet by acetylenic ($-C \equiv C-$) linkages to form the α -GY system. For this reason, we named these systems α -R57a-, α -H567-, and α -R57b-GYs. Our findings show that the high porosity nature of these GYs allows the chemical bonds to rearrange over the molecular plane, distributing tensions along the acetylenic chains, and resulting in a narrow distribution of bond lengths. In addition, the three systems maintain the metallic character of their full- sp^2 counterparts.

The rest of the paper is structured as follows. In the next section, we describe the theoretical methods employed in our simulations. In the subsequent two sections, the structural and electronic properties from the proposed NC-GYs are then presented and discussed. The paper ends with conclusions and implications.

II. THEORETICAL METHODS

We performed electronic structure simulations based on density functional theory (DFT) [44,45] as implemented in the SIESTA code [46]. The Perdew-Burke-Ernzerhof (PBE) functional was chosen to describe exchange correlation effects through the generalized gradient approximation (GGA) [47]. Core electrons were substituted by norm-conserving Troullier-Martins *ab initio* pseudopotentials [48]. Valence electronic wave functions were expanded according to a double- ζ polarized (DZP) basis, and a 400 Ry cutoff was used to represent the electronic charge on the real space. A 20 Å minimal spacing was introduced along the direction orthogonal to the systems' planes in order to avoid spurious interactions with periodic images of the structure. For k -space integrations, we used a benchmark corresponding to 46 Monkhorst-Pack points along the direction of the shortest lattice vector from all the studied systems. The number of k points for any other vector in any other system is then chosen according to this reference value so as to maintain grids with the same density of points for all structures.

The phonon dispersion curves of the studied membranes were calculated based on the finite displacement method as implemented in the PHONOPY code [49,50]. The crystal symmetries of the equilibrium structures were identified with the ISOTROPY package [51,52]. Two different $3 \times 2 \times 1$ supercells with 384 carbon atoms were constructed for the α -R57a and α -R57b -GY systems, while a $2 \times 2 \times 1$ supercell containing 256 carbons was considered for the α -H567-GY structure. These large supercells have to be used to guarantee that the force-constant matrix elements fall off to negligible values

TABLE I. Lattice parameters (in Å), bond-length range (in Å), space groups, number of atoms per area (in atoms/Å²), and formation energies (in eV/at) for *conventional* and NC GYs, GDY, TP-GYD, a polyynes chain, haeckelites, and graphene.

System	Lattice parameter (Å)	Bond-length range (Å)		Space groups	ρ (atoms/Å ²)	E_{form} (eV/at)
		$sp-sp$	$sp-sp^2$			
α -R57a	a = 16.60; b = 21.10	1.248 ± 0.002	1.411 ± 0.006	<i>cmm2</i>	0.183	1.080
α -R57b	a = 13.49; b = 25.96	1.248 ± 0.002	1.410 ± 0.004	<i>pgg2</i>	0.183	1.077
α -H567	a = b = 20.03	1.248 ± 0.003	1.410 ± 0.005	<i>p31m</i>	0.184	1.081
α -GY	a = b = 7.05	1.247	1.410	<i>p6mm</i>	0.186	1.059
β -GY	a = b = 9.58	1.249	1.403	<i>p6mm</i>	0.227	0.954
γ -GY	a = b = 6.95	1.239	1.422	<i>p6mm</i>	0.287	0.717
GDY	a = b = 9.56	1.286	1.411	<i>p6mm</i>	0.228	0.884
TP-GYD	a = b = 13.91	1.246	1.420	<i>p3m1</i>	0.215	0.440
Polyynes	a = 2.60	1.284/1.320	—	—	—	1.187

System	Lattice parameter (Å)	Bond length range (Å)		Space groups	ρ (atoms/Å ²)	E_{form} (eV/at)
		sp^2-sp^2				
R57a	a = 5.90; b = 7.53	1.442 ± 0.041		<i>cmm2</i>	0.360	0.243
R57b	a = 4.79; b = 9.23	1.441 ± 0.031		<i>pgg2</i>	0.362	0.225
H567	a = b = 7.14	1.442 ± 0.039		<i>p31m</i>	0.363	0.239
Graphene	a = b = 2.48	1.435		<i>p6mm</i>	0.376	0.000

at their boundaries. Atomic displacements of 0.02 Å were applied to obtain forces from the SIESTA package, from which the harmonic force constants were calculated.

We also performed Born-Oppenheimer molecular dynamics (BO-MD) simulations within SIESTA using $2 \times 2 \times 1$ supercells for the NC α -GYs proposed herein in order to check their thermal stability. A total simulation time of 2 ps was considered, with a 0.5 fs time step, at temperatures of 400 and 1000 K. The *NVT* (canonical) ensemble was used, and the thermostat was chosen according to the Nosé scheme.

III. STRUCTURE AND STABILITY

The crystalline structures of α -R57a-, α -H567-, and α -R57b-GYs are shown in Figs. 1(b)–1(d), respectively, along with a representation of the corresponding wallpaper symmetry groups for each structure. The α -R57a-GY sheet has a larger set of symmetry operations than its α -R57b-GY counterpart, so that it belongs to the *cmm2* group. On the other hand, α -R57b-GY fails to show mirror symmetry and belongs to the *pgg2* group, as it still features a set of glide planes. The schematic representations of these groups are illustrated in Figs. 1(b) and 1(d), respectively. For the α -H567-GY layer, we verify that it has *p31m* symmetry, which is different from graphene (*p6mm*), since α -H567-GY does not show a C_6 rotation axis. This symmetry group is illustrated over the hexagonal system's structure in Fig. 1(c). For the sake of convention, we consider the O_x and O_y axes composing the molecular plane, with O_z being the direction orthogonal to the membranes. The relaxed atomic positions of the three studied structures, together with their optimized lattice vectors, are reported in the Supplemental Material [53].

The α -R57a-GY and α -R57b-GY systems show different a and b lattice parameters for their rectangular lattices (as listed in Table I), in analogy with their full sp^2 counterparts. After full structural optimization, the areas for their unit cells are very similar (350.26 and 350.20 Å² for α -R57a-

GY and α -R57b-GY, respectively). The hexagonal lattice for α -H567-GY has a lattice constant of 20.03 Å. We note that the primitive cell area is 347.04 Å², which is similar to the rectangular cells from the previous cases. This is expected since the three systems have the same number of atoms in their unit cells, as well as the same proportion between sp and sp^2 atoms. Consequently, their numbers of atoms per area (ρ) are very similar to each other, as listed in Table I. In addition, these ρ values are comparable to that of *conventional* α -GY (see Table I), which also has the same ratio between the number of sp and sp^2 atoms.

In Fig. 2 we plot the charge density for the three proposed systems. In all cases, the acetylenic bonds ($sp-sp \approx 1.24$ Å) exhibit a larger electronic density than those links that involve the single bond ($sp-sp^2 \approx 1.41$ Å), which is consistent with

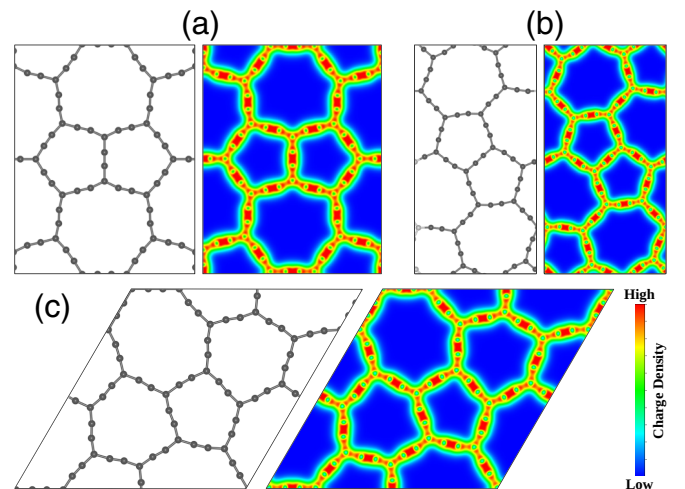


FIG. 2. Atomic structures of the unit cells and corresponding contour plot for the total electron density for (a) α -R57a-GY, (b) α -R57b-GY, and (c) α -H567-GY.

the nature of short triple bond lengths between carbon atoms. These results are in good agreement with other theoretical works [29,54], and the variance of the bond lengths can be seen in Table I. The narrow windows for bond lengths shown by NC α -GYs are allowed due to their high porosity. The pores allow the chemical bonds to rearrange over the layer, distributing tensions along the acetylenic chains. This can be better analyzed when comparing the bond length range of haeckelites and α -GYs. In systems that have only sp^2 atoms, bond lengths vary within a broad range, with variances up to 0.041 Å (see Table I). Such a range is significantly larger than the bond-length window for either the C – C or C \equiv C bonds in the proposed α -GY counterparts. This is also true for the bond-angle values involving the sp^2 atoms in the NC α -GYs.

Previous works have shown that the acetylenic units offer high flexibility to the GYs structures [55]. However, the insertion of a great number of these units onto the system can significantly reduce the fracture stress and Young's modulus. In this regard, evaluating the NC α -GYs stability in order to understand the role of the C \equiv C chains is an important point to study. To evaluate the relative energetic stability of α -R57a-, α -R57b-, and α -H567-GYs, we computed formation energies per atom (E_{form}), according to the following expression:

$$E_{\text{form}} = \frac{E_t - NE_i}{N}, \quad (1)$$

where E_t is the system's total energy, E_i is the energy per atom in graphene, and N is the total number of atoms in the system's unit cell. The calculated E_{form} compared to similar carbon-based materials (containing sp - sp hybridization) are listed in Table I. Our calculations indicate that α -R57a-, α -R57b-, and α -H567-GY exhibit formation energies of 1.080, 1.077, and 1.081 eV/at, respectively. These values are quite close of those found for α -GY, around 1.059 eV/at (with differences within 0.02 eV/at). It is important to note that there is a clear trend for the formation energies from the proposed GY systems as well as from similar nanocarbon systems. This is related to the ratio $x = N_{sp}/(N_{sp} + N_{sp^2})$ of sp atoms in the system, where N_{sp} (N_{sp^2}) is the number of sp (sp^2) hybridized atoms in the structure. In this sense, we can look at the graphene sheet ($x = 0$) and to a polylyne chain ($x = 1$) as two extremes for this relation. Such a trend in E_{form} can be observed in Fig. 3, where we plot E_{form} as a function of x for the studied structures. Considering the 2D systems, namely graphene, α -, β -, γ -GYs, GDY, TP-GYD, and the NC α -GYs, their formation energy as a function of x for different structures approximately follows a linear relation $E_{\text{form}} = Ax$ relation, with $A = 1.37$ eV/at. We observe that all the NC GYs are more stable than a polylyne chain (which is found to be stable within nanotube structures) [56,57].

To study the dynamical stability of the predicted NC GYs, we computed their phonon dispersions, as shown in Fig. 4. For comparison purposes, we also computed the phonon band structure for the *conventional* α -GY. No imaginary phonon frequencies are observed for α -GY, α -R57a-GY, and α -H567-GY systems throughout the whole Brillouin zone, which indicates that those materials are dynamically stable at zero pressure. However, α -R57b-GY shows small imaginary phonon modes along the Γ -Y path, indicating that this lattice

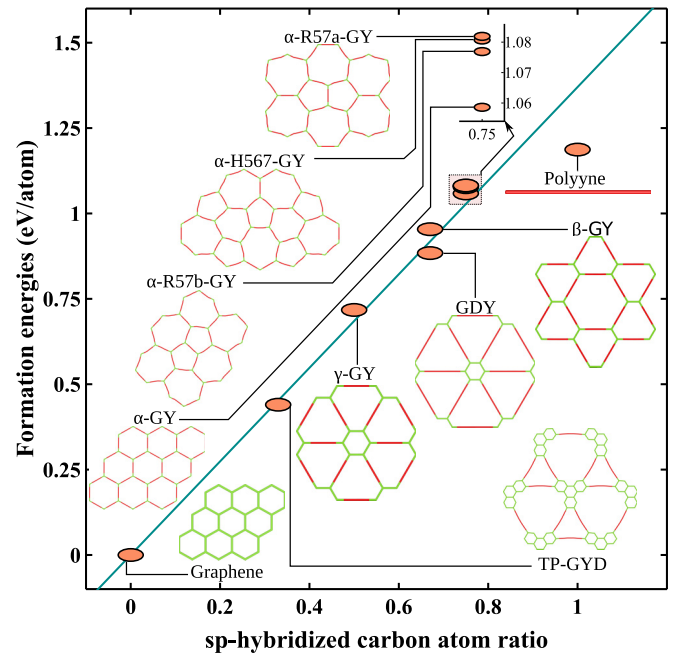


FIG. 3. Formation energy as a function of sp -hybridized carbon atom ratio (x) for different 2D carbon structures. Data for graphene, *conventional* and NC GYs, and GDY are fitted according to the $E_f = 1.37x$ formula, as indicated by the green line. In the atomic structures representations, bonds between sp hybridized carbons are represented in red, while sp - sp^2 bonds are represented in light green.

is slightly unstable. It is well known that the unstable eigenvectors (related to the imaginary phonon frequency) indicate the nature of the initial instability [58–60]. For the α -R57b-GY case, we verify that the eigenvectors of the imaginary modes correspond to out-of-plane vibrational motions. It turns out that a two-dimensional system can undergo non-negligible

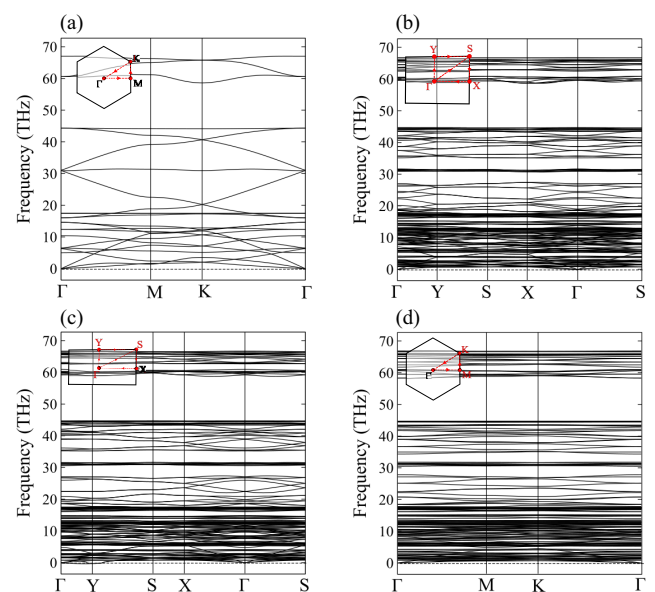


FIG. 4. Phonon band structures for (a) *conventional* α -GY, (b) α -R57a-GY, (c) α -R57b-GY, and (d) α -H567-GY.

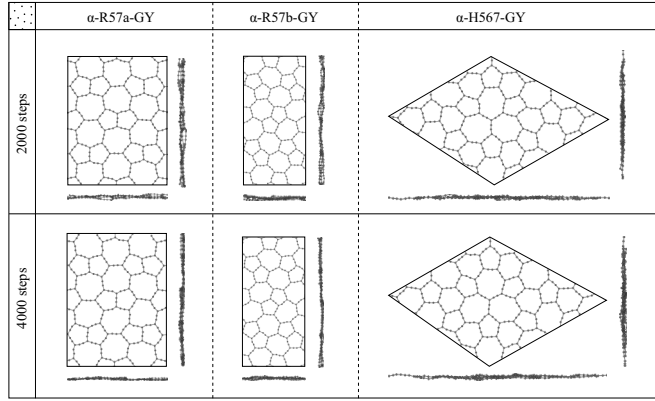


FIG. 5. Snapshots for the NC α -GY structures at the middle (2000 steps) and at the end (4000 steps) of the dynamics simulation for the three NC α -GYs: α -R57a-GY, α -R57b-GY, and α -H567-GY. Here we consider the temperature of 400 K. A similar scenario was observed for the structures at the temperature of 1000 K.

changes in the equilibrium interatomic forces once it is in a stacking configuration, of two or more layers, or when deposited over the top of a surface substrate. This is especially true if we consider the force components orthogonal to the molecular plane. Considering these aspects, we point out that α -R57b-GY can potentially be stabilized through proper orthogonal tensions in stacking configurations or when sustained over the substrate. While the stability of metallic carbon is usually very poor, recent works have shown metallic nanocarbon allotropes in two dimensions with metallic behavior exhibiting dynamical stability, as verified from theoretical calculations [61], and a clear synthesis route [43]. This indicates a good prospect for the future synthesis of the NC GYs proposed here.

We also performed BO-MD simulations to gain insight into the thermal stability of these NC α -GYs. During the simulation time, no system underwent structural reconstructions for the temperatures of 400 and 1000 K, as we observed no occurrence of bond breaking/formation during the dynamics according to a visual inspection. We illustrate this by showing snapshots for the NC α -GY structures at the middle (2000 steps) and at the end (4000 steps) of the dynamics simulation for 400 K in Fig. 5. Besides, these aspects can be quantified in terms of the Lindemann index [62,63]. The local Lindemann index δ_i , for any atom i in the structure, is given by

$$\delta_i = \frac{1}{n} \sum_{j \neq i} \frac{\sqrt{\langle d_{ij}^2 \rangle - \langle d_{ij} \rangle^2}}{\langle d_{ij} \rangle}, \quad (2)$$

where d_{ij} is the distance between atoms i and j . The averages are made over the simulation time. The sum in j is made through all the n atoms within a given cutoff radius r_L from the equilibrium position of atom i (excluding i). The system-average Lindemann index δ is given by

$$\delta = \frac{1}{N} \sum_i \delta_i, \quad (3)$$

where N is the total number of atoms in the structure. The δ , δ_i^{\min} , and δ_i^{\max} values for the three studied systems, as well

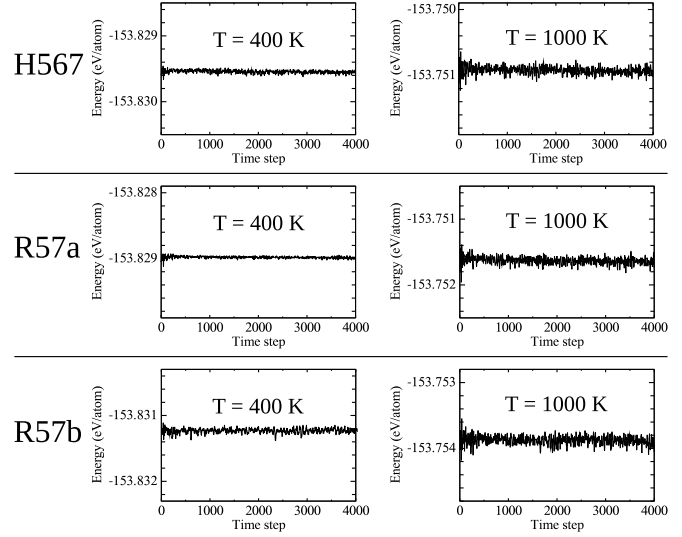


FIG. 6. Energy per atom as a function of time for the α -H567-GY, α -R57a-GY, and α -R57b-GY systems at the temperatures of 400 and 1000 K (left- and right-hand side panels, respectively).

as for α -GY, were below an upper threshold of 0.0314 for $r_L \geq 2.0 \text{ \AA}$ considering the simulations at 400 K. This is very close to a reference value for carbon nanotubes, which lies around 0.03 [64]. For the simulations at the higher temperature (1000 K), the δ , δ_i^{\min} , and δ_i^{\max} values were below an upper threshold of 0.0453 for the same r_L range.

In addition, we plot the total energy per atom as a function of time for the three NC GYs at the temperatures of 400 and 1000 K in Fig. 6. As expected, stronger energy fluctuations are observed in the simulation at 1000 K in comparison to the 400 K case. However, no dramatic changes are observed in these energy profiles, further indicating that the systems maintain their integrity and are suggested to be stable up to the temperature of 1000 K.

We also tested the mechanical stability of NC GYs by addressing the effects of lattice distortion to these systems. We applied, separately, uniaxial strain along the x - and y -axes by varying the lattice parameters of the fully relaxed system and fixing the supercell, while relaxing the atomic coordinates. Strain $\varepsilon_{xx}/\varepsilon_{yy}$ along the x/y directions is defined by

$$\varepsilon_{xx} = \frac{l_x - l_x^0}{l_x^0}, \quad \varepsilon_{yy} = \frac{l_y - l_y^0}{l_y^0}, \quad (4)$$

where l_i^0 (l_i) is the relaxed (strained) supercell size for the $i = x, y$ direction. We also applied equibiaxial strain by varying simultaneously both ε_{xx} and ε_{yy} maintaining $\varepsilon_{xx} = \varepsilon_{yy}$. This is trivially done for the rectangular systems, while we use a rectangular conventional supercell for the hexagonal structure. In all cases we varied ε_{xx} and ε_{yy} according to the -0.010 , -0.005 , 0 , $+0.005$, and $+0.010$ values. The elastic strain energy $U(\varepsilon)$ is defined as the energy difference (per unit area) between the strained and relaxed membranes [20]. It is written in terms of the strain components by

$$U(\varepsilon) = \frac{1}{2} C_{11} \varepsilon_{xx}^2 + \frac{1}{2} C_{22} \varepsilon_{yy}^2 + C_{12} \varepsilon_{xx} \varepsilon_{yy} + 2C_{66} \varepsilon_{xy}^2. \quad (5)$$

TABLE II. Components C_{11} , C_{22} , and C_{12} of the elastic modulus tensor for the three NC GYs. All values are given in N/m.

	C_{11} (N/m)	C_{22} (N/m)	C_{12} (N/m)
α -R57a	85.7	84.6	75.1
α -R57b	87.0	72.4	62.7
α -H567	86.2	86.0	73.8

Here, C_{11} , C_{22} , C_{12} , and C_{66} are the components of the elastic modulus tensor, for which we used the standard Voigt notation, with 1- xx , 2- yy , and 6- xy [65]. We obtain C_{11} and C_{22} by a least-squares fitting of the data for the uniaxial strain load along the x and y directions, respectively. These values are listed in Table II. We observe that α -R57a and α -H567 have isotropic mechanical properties, since the difference between C_{11} and C_{22} is below 1.5%. A least-squares fitting applied to the equibiaxial data gives $C_{12} + (C_{11} + C_{22})/2$, from which we obtain the C_{12} values listed in Table II. Considering uniaxial and biaxial strain, the material's elastic constants have to obey the corresponding Born-Huang criteria [20,66,67], namely $C_{11}C_{22} - C_{12}^2 > 0$ and $C_{66} > 0$, in order to be mechanically stable. In the case of isotropic systems ($C_{11} \approx C_{22}$), we have $2C_{66} = C_{11} - C_{12}$, so that the second stability criterion reduces to $C_{11} > C_{12}$ [65,67]. Considering the data from Table II and the above-mentioned criteria, α -R57a and α -H567 are mechanically stable. In the particular case of the α -R57b structure, we further applied the -0.010 , -0.005 , 0 , $+0.005$, and $+0.010$ values for the ε_{xy} shear stress, obtaining a positive value for C_{66} (1.39 N/m). Together with the data from Table II, this result shows that α -R57b obeys both Born-Huang rules, indicating that all the studied NC GY systems are mechanically stable.

These results suggest strongly that the structures proposed here are suitable to exist under laboratory conditions.

IV. ELECTRONIC PROPERTIES

Regarding electronic properties, we start by revisiting the *conventional* GY structures: α -, β -, and γ -GYs. In Fig. 7 we illustrate their atomic structures, with sp^2 (sp) atoms represented in light green (red), together with the corresponding electronic band structures plotted along high-symmetry lines of the Brillouin zone (BZ), a surface representation for their frontier bands over the entire BZ, and their density of states (DOS) split into partial (PDOS) sp and sp^2 contributions. As known previously [19,23,68,69], α - and β -GY are zero-gap semiconductors featuring a set of Dirac cones. In the α case, these cones lie at the vertices of the BZ. In addition, the local band minimum/maximum for the valence/conduction bands at the M point of the Brillouin zone are responsible for the two van Hove singularities in the DOS close to E_F , at $-0.70/ +0.76$ eV, respectively. For β -GY, the cones show up at a lower symmetry point, along the Γ to M path. In this system, we observe a set of four singularities close to the Fermi energy (E_F), with two being originated by the local band minimum/maximum for the valence/conduction bands at the M point of the BZ, and the other two (the most prominent ones) corresponding to the local band maximum/minimum for the valence/conduction bands along the Γ - K path. From the PDOS data for α - and β -GYs, we note that all the atoms take part in the frontier states, but with a larger contribution from the sp ones. In addition, we have a pair of bands with very low dispersion below -2.5 eV for α -GY. These levels are inside the -2.9 to -2.6 eV energy region, where the electronic states originate predominantly from sp atoms, as

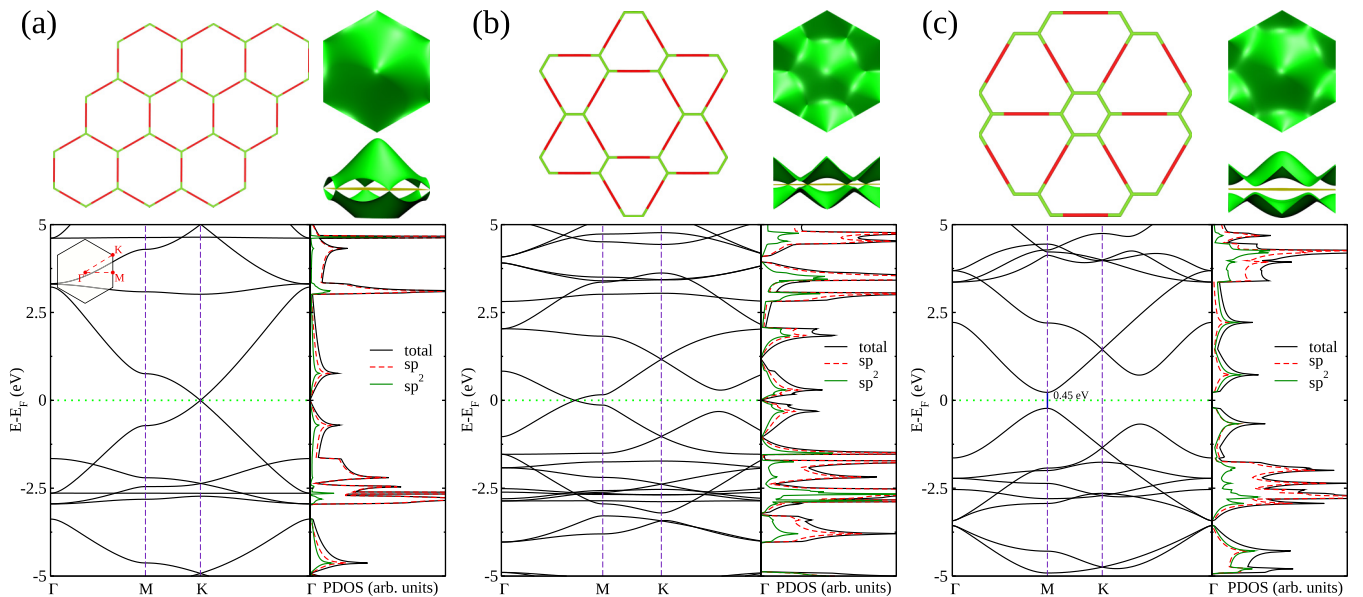


FIG. 7. Atomic structure, band structure, and corresponding density of states (DOS, full black line) split into partial DOS contributions (PDOS) for sp (dotted red line) and sp^2 (full green line) atoms for (a) α -GY, (b) β -GY, and (c) γ -GY. The inset in (a) represents a schematic illustration of the Brillouin zone highlighting the high-symmetry points. In the atomic structures, bonds between sp hybridized carbon atoms are represented in red, while sp - sp^2 bonds are represented in light green. In each case we also show the plots (green surfaces) of the frontier bands over the entire Brillouin zones according to lateral and top views (the Fermi level is represented by the yellow planes).

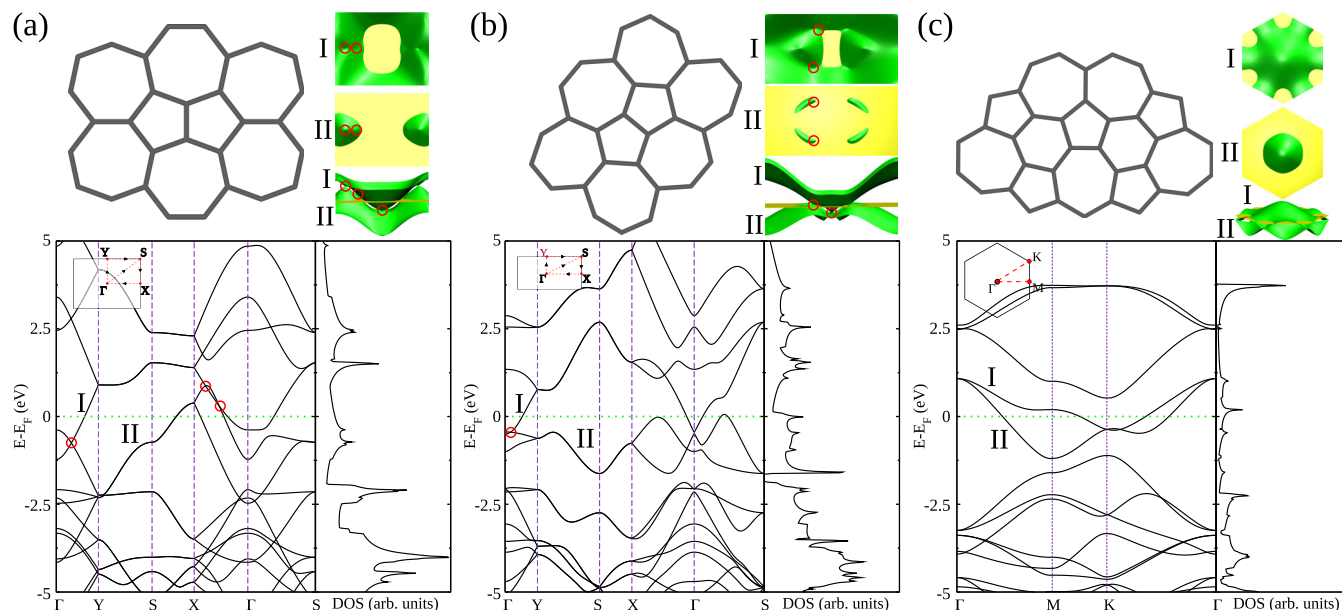


FIG. 8. Atomic structure, band structure, and corresponding density of states (DOS) for (a) R57a, (b) R57b, and (c) H567 full- sp^2 haeckelite structures. In each case we also show the plots (green surfaces) of the frontier bands over the entire Brillouin zones according to lateral and top views (the Fermi level is represented by the yellow planes). In (a) and (b), the red circles represent the cone intersections between the frontier bands I and II.

seen from the PDOS spectrum. A similar scenario also occurs for the β -GY system.

The γ -GY case behaves differently, showing a 0.45 eV band gap consistent with previous literature [19,69–71]. PDOS data show that sp and sp^2 atoms contribute evenly to the valence-band maximum of γ -GY, while the conduction-band minimum has a slightly higher component from sp^2 carbons. This is consistent with the fact that γ -GY has the larger proportion of sp^2 atoms from all three *conventional* GYs. As in β -GY, the most prominent DOS peaks around the Fermi energy are due to the local band maximum/minimum for the valence/conduction bands along the Γ -K line of the BZ. The γ -GY sheet also shows a significant contribution from sp^2 atoms for localized levels around -2.5 eV, but which have a predominantly sp character.

An important characteristic of graphyne systems in comparison to full- sp^2 graphene is how electrons are delocalized in the structure. Since frontier states are distributed not only on tricoordinated (sp^2) atoms but also on dicoordinated (sp) atoms, band dispersion is significantly reduced in GY structures. For instance, we can look at the bands crossing the Fermi level (E_F) for graphene and α -GY. If we compute the total dispersion between the bottom/top of the frontier valence/conduction bands, this corresponds to a 14.43 eV energy range for graphene, which is reduced to 5.04 eV for α -GY. This dispersion is even narrower for β -GY (2.70 eV), as this system has a more intricate distribution of hexagonal- and triangular-truncated pores.

Another common feature of these graphyne structures is the strong contribution from the sp atoms to the DOS at energy ranges around -2.5 eV. As we will discuss later, these sets of states are also present in the NC GYs and they are

related to those π bonds, from the $C \equiv C$ links, which lie over the molecular plane.

Before moving into the NC GY systems, we also revisit the electronic structure of the full sp^2 R57a, R57b, and H567 sheets. They have their electronic band structure along special lines of the BZ and their DOS shown in Fig. 8. In this figure, we also plot a surface representation of their frontier bands over the entire BZ. As known previously [15,16,32], all these systems display a metallic behavior, with a broad range of energy values with nonzero DOS around the Fermi level. In the R57a case, one of the frontier bands crosses E_F along a closed curve of k -points around Γ in the reciprocal space, as can be seen from an upper view of this band in Fig. 8(a), with a minimum at $E < E_F$ energies. The other frontier band crosses the Fermi energy around the X point of the BZ, with maxima at $E > E_F$ energies. These bands are marked as I and II, respectively, on the plot along the high symmetry lines from Fig. 8(a). We also observe that these two bands cross each other according to a set of six cones: four along the Γ -X direction, symmetrically positioned around Γ , and two along the Γ -Y path, also symmetrical relative to Γ . Some of these cone positions are represented by the red circles in Fig. 8(a).

The R57b system also features a pair of bands crossing E_F , with one of them [marked as I in Fig. 8(b)] having $E = E_F$ for a closed k -space curve around Γ . The other branch [marked as II in Fig. 8(b)] passes by E_F at four k -space regions, each on a quadrant of the BZ. These two bands also cross each other according to six cones, but in different positions of the BZ compared to the R57a case: two along the Γ -Y path and the other four at lower symmetry k -points (one in each quadrant of the BZ). Part of these points is marked by the red circles in Fig. 8(b). Another noticeable difference to the previous

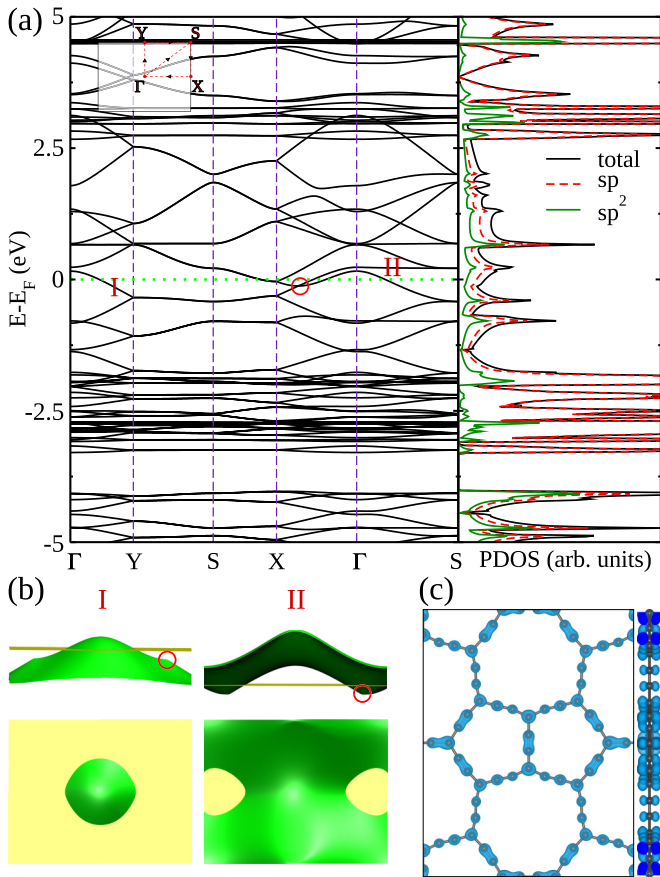


FIG. 9. Band structure along the high-symmetry lines of the BZ and the corresponding DOS and PDOS for the α -R57a-GY structure. The sp and sp^2 PDOS contributions are represented by the dotted red and solid green lines, respectively, with the total DOS represented by the black full line. (b) Plots for the frontier bands (green surfaces) over the entire BZ. The Fermi level is represented by the yellow plane. (c) Partial charge plot around the Fermi level energy. An isovalue of $0.0004 \text{ e}\text{\AA}^{-3}$ was used. In (a) and (b), the red circles represent the cone intersections between the frontier bands I and II.

R57a structure is the occurrence of a band gap from -1.83 to -1.67 eV , below the Fermi energy.

For the H567 case, we also note a pair of bands crossing the Fermi level [marked as I and II in Fig. 8(c)]. Although these two bands do not cross any other electronic band-structure branches, we observe no energy gaps below/above their bottom/top energy values, respectively. In other words, they share part of their energy ranges with other bands but with no crossing at the k -space. This is a different feature compared to the rectangular systems, where the frontier bands cross with other branches of the electronic structure at some points of the BZ. As we discuss below, the corresponding states in the α -H567-GY have a more localized character, opening small gaps in their vicinity.

Now we discuss the results for NC GYs. In Fig. 9(a) we plot the electronic band structure for α -R57a-GY along the high-symmetry lines of the BZ together with the corresponding DOS and PDOS contributions from sp and sp^2 atoms. As its full- sp^2 counterpart, this is a metallic system, with one band crossing the Fermi level along the Γ -X, Γ -Y, and Γ -S

paths. Such a band [marked as I in Fig. 9(a)] has a maximal value for $E > E_F$ energies at Γ and it is “cut” by the Fermi energy at a set of k -points around a closed curve similar to a circle around $k = 0$ (Γ point), as observed in the surface plot for this band over the entire BZ in Fig. 9(b). This feature indicates that this sheet should result in metallic systems once cast into a nanotube structure. This can be understood in terms of a zone folding approach, as we will always have a cutting line passing through this $E = E_F$ circle in the k -space, no matter which is the nanotube chirality. There is a second band [indicated by II in Fig. 9(a)] that crosses E_F along the Γ -X path. In fact, we have $E = E_F$ states along a closed k -space curve around the X point of the BZ for this band. Interestingly, these two α -R57a-GY bands are similar to the frontier bands of R57a in the sense of the k -paths along which they cross the Fermi level, except that they look inverted along the energy axis in comparison to each other. Namely, for the α -R57a-GY’s band I crossing E_F around Γ , the states around $k = 0$ lie above E_F , while the corresponding states for the R57a’s band I lie below E_F . The same analysis can be made for the other frontier bands from R57a (band II) and α -R57a-GY (band II), crossing the frontier energy around the X point. We will discuss this point later, as we observe similar behavior for the other NC GYs. Still comparing these two systems, the two frontier bands for α -R57a-GY cross each other only at two points of the BZ, along the Γ -X path and symmetrically positioned relative to Γ , as indicated by the red circles in Figs. 9(a) and 9(b). This is different for R57a, where we observe a total of six such conelike crossings.

In Fig. 9(a) we also plot the DOS (black full line) together with the PDOS split over the sp (dashed red line) and sp^2 (full green line) atoms separately for α -R57a-GY. Note that both sp and sp^2 atoms contribute to the frontier states around E_F , but with predominance for sp carbon, as we have three sp atoms for each sp^2 one. The major contribution from the sp atoms is due to π states, as indicated in Fig. 9(c), where we plot the partial charge integrated for a 0.1 eV interval around the Fermi level. A side view of this cloud shows a node over the entire molecular plane. For example, this shows that we have no contribution from the orbitals composing those π bonds from the $\text{C} \equiv \text{C}$ link which lie over the molecular plane (those involving p_x and/or p_y orbitals). In addition, while the partial charge cloud is highly delocalized, its major contribution comes from chains linking sp^2 atoms inside the pentagonal pores.

The α -R57a-GY system has a nonzero DOS profile for a wide range of energy values around the Fermi level, indicating availability of states for a broad energy window. Considering device applications, this is suggestive that the NC GY structure can potentially act as an efficient electrode for electronic transport in nanojunction setups [72,73]. Such structural elements allow device development to be focused on the properties of the junction itself, usually involving small molecules or other finite-sized structures [73–76]. We highlight that additional calculations (beyond the scope of this work) are necessary to address these points for particular nanojunction setups.

Further examining the α -R57a-GY DOS, the imbalance between sp and sp^2 contributions is remarkably more intense for the energy range from -3.05 to -1.95 eV , which is dominated

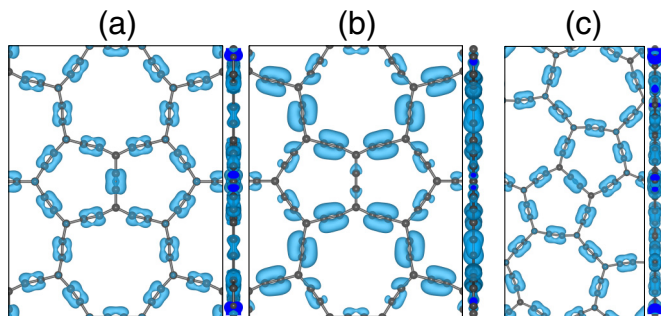


FIG. 10. Partial charge plots for α -R57a-GY at the (a) -1.95 eV and (b) -3.05 eV energy points, and for (c) -2.0 eV in α -R57b-GY. An isovalue of $0.005 e\text{\AA}^{-3}$ for (a) and (c) was used, and of $0.002 e\text{\AA}^{-3}$ for (b).

by several bands' branches with very low dispersion. We note that the previously studied α -, β -, and γ -GYs also display similar features, as they all have a set of low dispersive bands for energies around/close to -2.5 eV, as can be seen by their electronic band structures shown in Fig. 7. Such levels in the graphyne layers are associated with one of the π bonds from the acetylenic unit, namely the one over the xy plane. This is illustrated in Figs. 10(a) and 10(b), where we show the partial charge plot for the α -R57a-GY system around the -1.95 and -3.05 eV energy values, respectively, according to both top and side views. From the side views, we note that these states do not have a nodal plane coincident with the xy molecular plane, as it occurs for the states around E_F shown in Fig. 9(c). Rather, they are spread over the lateral regions of the $C \equiv C$ bonds. We will hereafter refer to these as π_{xy} bonds, with the other bond related to the p_z orbitals from the acetylenic chain being referred to as π_z . We will come back to this point at the end of this section, after discussing the electronic properties of the other NC GYs, as this is indirectly associated with the inversionlike behavior for the frontier bands of these GYs in comparison with their sp^2 counterparts.

Finally, in the α -R57a-GY bands' profile from Fig. 9(a), we note that bands are all degenerated two-by-two along the Y - S - X path of the BZ. Such is also observed for the R57a sp^2 system. This particular feature originated from the choice of a rectangular conventional cell for a centered rectangular system. While the conventional unit vectors are given by

$$\mathbf{a}_1^c = (a, 0) \quad \text{and} \quad \mathbf{a}_2^c = (0, b), \quad (6)$$

the primitive lattice vectors for the centered rectangular lattice can be written as

$$\mathbf{a}_1^p = \left(\frac{a}{2}, \frac{b}{2} \right) \quad \text{and} \quad \mathbf{a}_2^p = \left(\frac{a}{2}, -\frac{b}{2} \right). \quad (7)$$

In Fig. 11(a) we draw the BZ corresponding to the primitive (the larger zone in red) and to the conventional cell (the smaller zone in blue). Once we fold the primitive BZ over the conventional one [as illustrated in Fig. 11(b)], we have the patterns in green in Fig. 11(a), formed by the edges of the primitive zone. On the other hand, the folded edges from the primitive cell lie along the X - S and S - Y paths of the conventional cell, explaining why we have doubly degenerate bands' branches along these lines.

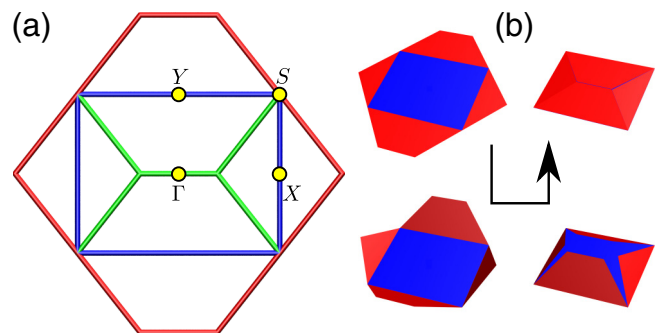


FIG. 11. (a) Representation for the primitive Wigner-Seitz cell of the reciprocal space of a centered rectangular system (hexagon in red), together with the corresponding conventional cell (blue rectangle). The lines in green represent the edge of the primitive cell when folded over the conventional one. The high-symmetry points of the conventional cell are represented by Γ , X , Y , and S . (b) Schematic illustration for how one can fold the primitive cell over the conventional counterpart.

The α -R57b-GY layer is also metallic, as verified from its electronic band-structure plot along the high-symmetry lines of the BZ in Fig. 12(a). We also plot its frontier bands over the entire BZ in Fig. 12(b). As in its R57b sp^2 counterpart, a band crosses E_F around a closed k -space curve around the Γ point. For this reason, one expects that hypothetical α -R57b-GY nanotubes (as in the α -R57a-GY case) should all be metallic, except for high curvature tubes, for which zone folding does not give a good description [76]. This frontier band is marked as I in Fig. 12(a), and it is shown by the surface plot in Fig. 12(b). The following band above the Fermi level [marked as II in Fig. 12(a)] also has its surface plot illustrated in Fig. 12(b). Note that band II has two symmetrically located minima along the Γ - X path at an energy value only 2 meV above E_F . These two frontier bands have geometric characteristics similar to the corresponding bands in the sp^2 counterpart system, except by an inversion over the energy axis. To be more specific, the band crossing E_F around Γ for α -R57b-GY has $E > 0$ at $k = 0$, while the corresponding band from R57b at $k = 0$ has a negative energy value. As we discussed earlier, a similar inversion occurs in α -R57a-GY relative to R57a.

From the α -R57b-GY DOS plot [split on sp and sp^2 atom contributions in Fig. 12(a)] we also note that sp states have a larger contribution than sp^2 levels near the Fermi energy. A different feature of α -R57b-GY in comparison to α -R57a-GY is the appearance of small band gaps around 0.52 and -0.58 eV relative to E_F . Note that this is also different from its full sp^2 R57b counterpart, which shows only a forbidden energy region below E_F (around -1.75 eV). This is an interesting characteristic which potentially can result in nonlinear transport properties, especially because these gaps are closer to E_F in α -R57b-GY compared to the one in the R57b sheet.

We also plot the partial charge integrated for a 0.1 eV energy interval around E_F for α -R57b-GY. We note that differently from the α -R57a-GY structure, the acetylenic chains in linking pairs of pentagonal pores show a contribution similar to the links within the pentagons. On the other hand,

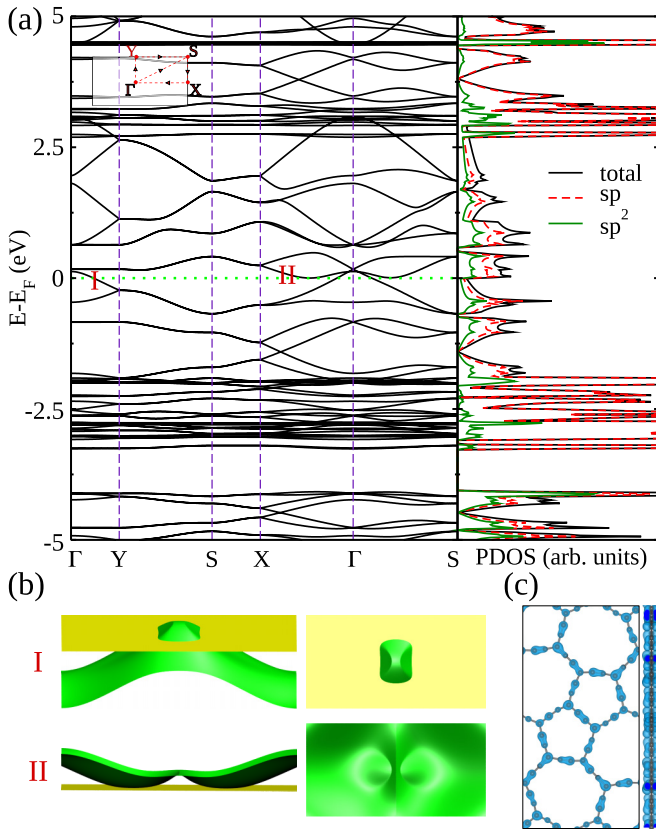


FIG. 12. Band structure along the high-symmetry lines of the BZ and the corresponding DOS and PDOS for the α -R57b-GY structure. The sp and sp^2 PDOS contributions are represented by the dotted red and solid green lines, respectively, with the total DOS represented by the black full line. (b) Plots for the frontier bands (green surfaces) over the entire BZ. The Fermi level is represented by the yellow plane. (c) Partial charge plot around the Fermi level energy. An isovalue of $0.0004 \text{ e}\text{\AA}^{-3}$ was used.

as in the α -R57a-GY case, this system also shows a set of localized states for energies below -2.0 eV , which come mostly from the π_{xy} bonds from the acetylenic groups, as illustrated by the partial charge plot at this energy value in Fig. 10(c).

Interestingly, this system also shows electronic bands degenerated two-by-two along the X - S - Y paths, even though the rectangular cell is the primitive one. This is due to the glide plane symmetries in the structure [see Fig. 1(d)]. Note that the pair of pentagonal pores in the center of the cell is reflected (over either the x or y direction) relative to the pairs of five-membered pores in the corners of the same cell. This symmetry is also observed in the full- sp^2 R57b structure [see its band structure in Fig. 8(b)].

The α -H567-GY system is also metallic, with a pair of bands crossing the Fermi level, as seen from its band structure plotted along the high-symmetry lines in Fig. 13(a). As in the sp^2 H567 system, these two bands do not cross any other branch of the electronic structure, as further illustrated by their plots over the entire BZ in Fig. 13(b). Further, as these two bands have significantly lower dispersion due to the distribution of acetylenic bonds, this GY system features

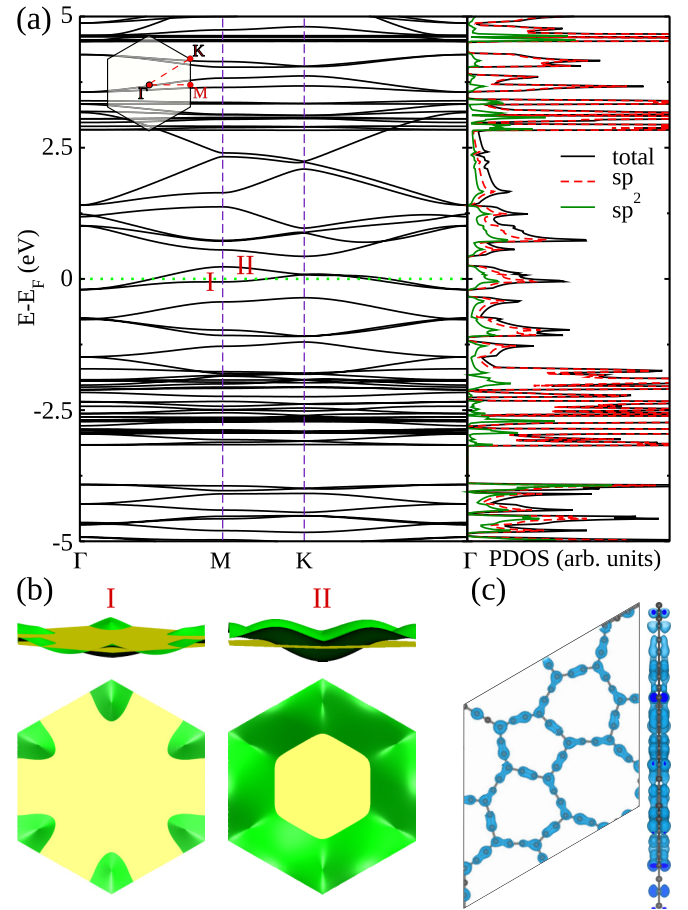


FIG. 13. Band structure along the high-symmetry lines of the BZ and the corresponding DOS and PDOS for the α -H567-GY structure. The sp and sp^2 PDOS contributions are represented by the dotted red and solid green lines, respectively, with the total DOS represented by the black full line. (b) Plots for the frontier bands (green surfaces) over the entire BZ. The Fermi level is represented by the yellow plane. (c) Partial charge plot around the Fermi level energy. An isovalue of $0.0007 \text{ e}\text{\AA}^{-3}$ was used.

small band gaps both below and above these frontier states. This is a lattice signature different from the H567 sp^2 counterpart and from the α -R57a- and α -R57b-GY systems. Such gaps close to the Fermi level have the potential to exert a strong influence on electronic transport setups having these systems as an underlying lattice, so that the choice of the GY lattice can be used as a strategic tool to tune these kinds of properties. As mentioned for the α -R57b-GY case (which features one such gap for energies below E_F), interesting nonlinear phenomena can take place in such systems. These include, for instance, negative differential resistance (NDR) effects, which can result from the particular band structure of electrodes [73,77,78]. Several examples have been reported in the literature, including graphynelike systems [24,79,80]. We then believe that the particularities in the electronic behavior of the three NC GYs proposed here can contribute to future developments in nanoelectronics. Furthermore, the atomic structure of such nanocarbons can be embedded in a variety of nanodevices with exotic architectures, an active and challenging field of research [72]. However, we highlight one

more time that further calculations, beyond the scope of this work, are necessary to fully elucidate this point. Regarding the states around E_F , these are highly delocalized and have a nodal plane coincident with the molecular plane, as illustrated by the partial charge plot around E_F , shown in Fig. 13(c). On the other hand, a partial charge plot (not shown) for the flat levels around -2.5 eV shows that they correspond to the π_{xy} bonds from $C \equiv C$, as observed for the other GY structures.

The two frontier bands in α -H567-GY [marked as I and II in Figs. 13(a) and 13(b)] have a common minimum value at the Γ point, while the corresponding bands in the sp^2 H567 sheet have a common maximum value at the same point of the k -space. Such inversion is similar to what happens for the frontier bands in the rectangular NC GYs. Now we discuss how this energy inversion of the frontier bands in NC GY relative to haeckelites can be associated with a topological consequence of introducing acetylenic chains between the sites of the sp^2 lattice. To understand this, we make a connection with the localized states around -2.5 eV observed for all the studied GY structures. As we discussed before, these are associated with the π_{xy} bonds. The localized aspect from these states is a consequence of symmetry, since the p_x , p_y , and s orbitals are even relative to the z direction. Meanwhile, the p_z wave functions are odd relative to this same direction. Consequently, the π_{xy} bond orbitals do not overlap with the π states from the neighboring sp^2 atoms but are rather localized at the $C \equiv C$ links. The energy range of these π_{xy} states indicates that this localization results in stronger bonding than the π_z ones, as they are moved away from the Fermi level. On the other hand, the π_z bonds interact with the π states from the sp^2 atoms, as shown by the DOS and partial charge plots from Figs. 9, 12, and 13, so that they play a dominant role in the determination of the frontier states. This explains why π -band tight-binding (TB) models work so well for graphyne structures [81,82].

To illustrate this, we performed a simple π -band first-nearest-neighbor TB calculation for both H567 and α -H567-GY systems. In this simple model, we even considered the same $\gamma = -3$ eV hopping integral for both sp - sp and sp - sp^2 bonds. The TB electronic structures for these two systems are shown in Fig. 14. The TB bands around the Fermi level show remarkable similarity with the DFT results, reproducing the same result for the minimum/maximum position, relative to E_F , for the two systems. The capture of the frontier bands' inversion behavior with such a simple model indicates that this is a topological consequence of the insertion of additional sites between the tricoordinated sites of the lattice.

V. CONCLUSIONS

In summary, we proposed a set of *nonconventional* graphyne structures whose underlying lattices are predominantly

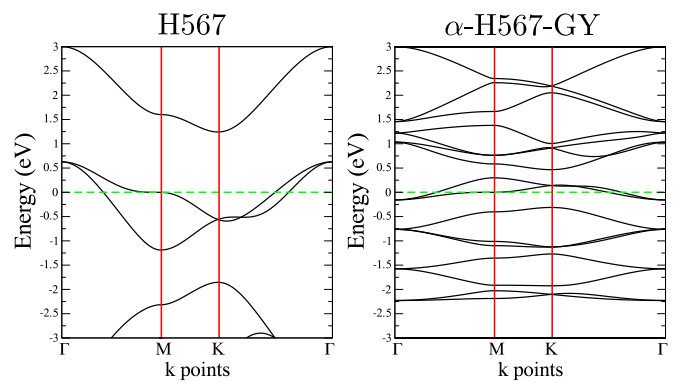


FIG. 14. Electronic band structure for H567 and for α -H567-GY along high-symmetry lines of the BZ according to a π -band first-nearest-neighbor TB calculation with a $\gamma = -3$ eV hopping parameter.

formed by pentagons and heptagons. We demonstrated that these nonhexagonal rings are better accommodated in graphyne networks rather than at full sp^2 configurations since the large extent of the structures with acetylenic chains allows for a better structural organization, reducing tensions and resulting in systems with a narrower bond-length range. Furthermore, the systems are shown to be stable as their formation energies are lower than recently synthesized graphyne-like structures. They also feature phonon band structures with an absence of imaginary frequency modes. BO-MD simulations also demonstrate structural stability at 400 K. Regarding their electronic structure, the three proposed graphynes are metallic but with marked differences to their full- sp^2 counterparts. In addition to opening forbidden energy regions in the vicinity of the Fermi level, the introduction of acetylenic links changes the profile of the frontier bands relative to the sp^2 parent structure, which could be understood in terms of simple model Hamiltonians. Then, these characteristic electronic signatures can offer different strategies to use these systems as components in nanodevice development, which is a realistic assumption given the recent developments in the synthesis of exotic nanocarbons in two dimensions.

ACKNOWLEDGMENTS

T.A.O. and P.V.S. acknowledge CAPES for scholarship support. E.C.G acknowledges support of the Brazilian agency CNPq (Process No. 429785/2018-6, and Process No. 310394/2020-1). P.V.S. and E.C.G. acknowledge support from the PROCAD 2013/CAPES program. The authors thank the Laboratório de Simulação Computacional Cajufina (LSCC) at Universidade Federal do Piauí for computational support. The authors also acknowledge support from CENAPAD-UFC at Universidade Federal do Ceará.

- [1] H. W. Kroto, J. R. Heath, S. C. O'Brien, R. F. Curl, and R. E. Smalley, C_{60} : Buckminsterfullerene, *Nature (London)* **318**, 162 (1985).
- [2] W. A. Chalifoux and R. R. Tykwinski, Synthesis of polyynes to model the sp -carbon allotrope carbyne, *Nat. Chem.* **2**, 967 (2010).

- [3] S. Iijima and T. Ichihashi, Single-shell carbon nanotubes of 1-nm diameter, *Nature (London)* **363**, 603 (1993).
- [4] K. S. Novoselov, Electric field effect in atomically thin carbon films, *Science* **306**, 666 (2004).
- [5] Y. Wu, J. Zhu, and L. Huang, A review of three-dimensional graphene-based materials: Synthesis and applications to

- energy conversion/storage and environment, *Carbon* **143**, 610 (2019).
- [6] A. K. Geim and K. S. Novoselov, The rise of graphene, *Nat. Mater.* **6**, 183 (2007).
- [7] I. W. Frank, D. M. Tanenbaum, A. M. van der Zande, and P. L. McEuen, Mechanical properties of suspended graphene sheets, *J. Vac. Sci. Technol. B* **25**, 2558 (2007).
- [8] A. H. Castro Neto, F. Guinea, N. M. Peres, K. S. Novoselov, and A. K. Geim, The electronic properties of graphene, *Rev. Mod. Phys.* **81**, 109 (2009).
- [9] F. Schwierz, Graphene transistors, *Nat. Nanotechnol.* **5**, 487 (2010).
- [10] A. V. Thomas, B. C. Andow, S. Suresh, O. Eksik, J. Yin, A. H. Dyson, and N. Koratkar, Controlled crumpling of graphene oxide films for tunable optical transmittance, *Adv. Mater.* **27**, 3256 (2015).
- [11] J. Lin, Z. Peng, Y. Liu, F. Ruiz-Zepeda, R. Ye, E. L. Samuel, M. J. Yacaman, B. I. Yakobson, and J. M. Tour, Laser-induced porous graphene films from commercial polymers, *Nat. Commun.* **5**, 5714 (2014).
- [12] R. Matsuoka, R. Toyoda, R. Shiotsuki, N. Fukui, K. Wada, H. Maeda, R. Sakamoto, S. Sasaki, H. Masunaga, K. Nagashio, and H. Nishihara, Expansion of the graphdiyne family: A triphenylene-cored analogue, *ACS Appl. Mater. Interfaces* **11**, 2730 (2019).
- [13] T. Wang, L.-X. Wang, D.-L. Wu, W. Xia, and D.-Z. Jia, Interaction between nitrogen and sulfur in co-doped graphene and synergetic effect in supercapacitor, *Sci. Rep.* **5**, 9591 (2015).
- [14] B. Ram and H. Mizuseki, C568: A new two-dimensional sp^2 - sp^3 hybridized allotrope of carbon, *Carbon* **158**, 827 (2020).
- [15] V. H. Crespi, L. X. Benedict, M. L. Cohen, and S. G. Louie, Prediction of a pure-carbon planar covalent metal, *Phys. Rev. B* **53**, R13303 (1996).
- [16] H. Terrones, M. Terrones, E. Hernández, N. Grobert, J. C. Charlier, and P. M. Ajayan, New Metallic Allotropes of Planar and Tubular Carbon, *Phys. Rev. Lett.* **84**, 1716 (2000).
- [17] Y. Liu, G. Wang, Q. Huang, L. Guo, and X. Chen, Structural and Electronic Properties of T Graphene: A Two-Dimensional Carbon Allotrope with Tetrarings, *Phys. Rev. Lett.* **108**, 225505 (2012).
- [18] X. Li, Q. Wang, and P. Jena, ψ -graphene: A new metallic allotrope of planar carbon with potential applications as anode materials for lithium-ion batteries, *J. Phys. Chem. Lett.* **8**, 3234 (2017).
- [19] J. Kang, Z. Wei, and J. Li, Graphyne and its family: Recent theoretical advances, *ACS Appl. Mater. Interfaces* **11**, 2692 (2019).
- [20] S. Zhang, J. Zhou, Q. Wang, X. Chen, Y. Kawazoe, and P. Jena, Penta-graphene: A new carbon allotrope, *Proc. Natl. Acad. Sci. USA* **112**, 2372 (2015).
- [21] B. Ram and H. Mizuseki, Tetrahexcarbon: A two-dimensional allotrope of carbon, *Carbon* **137**, 266 (2018).
- [22] R. H. Baughman, H. Eckhardt, and M. Kertesz, Structure-property predictions for new planar forms of carbon: Layered phases containing sp^2 and sp atoms, *J. Chem. Phys.* **87**, 6687 (1987).
- [23] D. Malko, C. Neiss, F. Viñes, and A. Görling, Competition for Graphene: Graphynes with Direction-Dependent Dirac Cones, *Phys. Rev. Lett.* **108**, 086804 (2012).
- [24] W. Wu, W. Guo, and X. C. Zeng, Intrinsic electronic and transport properties of graphyne sheets and nanoribbons, *Nanoscale* **5**, 9264 (2013).
- [25] G. Li, Y. Li, H. Liu, Y. Guo, Y. Li, and D. Zhu, Architecture of graphdiyne nanoscale films, *Chem. Commun.* **46**, 3256 (2010).
- [26] A. Rabia, F. Tumino, A. Milani, V. Russo, A. L. Bassi, N. Bassi, A. Lucotti, S. Achilli, G. Fratesi, N. Manini, G. Onida, Q. Sun, W. Xu, and C. S. Casari, Structural, electronic, and vibrational properties of a two-dimensional graphdiyne-like carbon nanonetwork synthesized on au(111): Implications for the engineering of sp - sp^2 carbon nanostructures, *ACS Appl. Nano Mater.* **3**, 12178 (2020).
- [27] N. V. R. Nulakani and V. Subramanian, Cp-graphyne: A low-energy graphyne polymorph with double distorted Dirac points, *ACS Omega* **2**, 6822 (2017).
- [28] W.-J. Yin, Y.-E. Xie, L.-M. Liu, R.-Z. Wang, X.-L. Wei, L. Lau, J.-X. Zhong, and Y.-P. Chen, R-graphyne: A new two-dimensional carbon allotrope with versatile dirac-like point in nanoribbons, *J. Mater. Chem. A* **1**, 5341 (2013).
- [29] S. Jana, A. Bandyopadhyay, and D. Jana, Acetylenic linkage dependent electronic and optical behaviour of morphologically distinct '-ynes,' *Phys. Chem. Chem. Phys.* **21**, 13795 (2019).
- [30] P. Serafini, A. Milani, D. M. Proserpio, and C. S. Casari, Designing all graphdiyne materials as graphene derivatives: Topologically driven modulation of electronic properties, *J. Phys. Chem. C* **125**, 18456 (2021).
- [31] A. Ivanovskii, Graphynes and graphdyines, *Prog. Solid State Chem.* **41**, 1 (2013).
- [32] M. Deza, P. W. Fowler, M. Shtogrin, and K. Vietze, Pentaheptite modifications of the graphite sheet, *J. Chem. Inf. Comput. Sci.* **40**, 1325 (2000).
- [33] J. Cai, P. Ruffieux, R. Jaafar, M. Bieri, T. Braun, S. Blankenburg, M. Muoth, A. P. Seitsonen, M. Saleh, X. Feng, K. Müllen, and R. Fasel, Atomically precise bottom-up fabrication of graphene nanoribbons, *Nature (London)* **466**, 470 (2010).
- [34] Q. Fan, D. Martin-Jimenez, D. Ebeling, C. K. Krug, L. Brechmann, C. Kohlmeyer, G. Hilt, W. Hieringer, A. Schirmeisen, and J. M. Gottfried, Nanoribbons with nonalternant topology from fusion of polyazulene: Carbon allotropes beyond graphene, *J. Am. Chem. Soc.* **141**, 17713 (2019).
- [35] J. Kotakoski, A. V. Krasheninnikov, U. Kaiser, and J. C. Meyer, From Point Defects in Graphene to Two-Dimensional Amorphous Carbon, *Phys. Rev. Lett.* **106**, 105505 (2011).
- [36] J. Tour, Top-down versus bottom-up fabrication of graphene-based electronics, *Chem. Mater.* **26**, 163 (2014).
- [37] M. Bieri, M. Treier, J. Cai, K. Ait-Mansour, P. Ruffieux, O. Groning, P. Groning, M. Kastler, R. Rieger, X. Feng, K. Müllen, and R. Fasel, Porous graphenes: two-dimensional polymer synthesis with atomic precision, *Chem. Commun.* **6919–6921**, 6919 (2009).
- [38] C.-A. Palma and P. Samori, Blueprinting macromolecular electronics, *Nat. Chem.* **3**, 431 (2011).
- [39] J. Cai, C. A. Pignedoli, L. Talirz, P. Ruffieux, H. Söde, L. Liang, V. Meunier, R. Berger, R. Li, X. Feng, K. Müllen, and R. Fasel, Graphene nanoribbon heterojunctions, *Nat. Nanotechnol.* **9**, 896 (2014).
- [40] J. R. Sanchez-Valencia, T. Dienel, O. Groning, I. Shorubalko, A. Mueller, M. Jansen, K. Amsharov, P. Ruffieux, and R.

- Fasel, Controlled synthesis of single-chirality carbon nanotubes, *Nature (London)* **512**, 61 (2014).
- [41] S. Mishra, J. Melidoni, K. Eimre, S. Obermann, O. Gröning, C. A. Pignedoli, P. Ruffieux, X. Feng, and R. Fasel, On-surface synthesis of super-heptazethrene, *Chem. Commun.* **56**, 7467 (2020).
- [42] R. S. K. Houtsma, J. de la Rie, and M. Stöhr, Atomically precise graphene nanoribbons: interplay of structural and electronic properties, *Chem. Soc. Rev.* **50**, 6541 (2021).
- [43] Q. Fan, L. Yan, M. W. Tripp, O. Krejčí, S. Dimosthenous, S. R. Kachel, M. Chen, A. S. Foster, U. Koert, P. Liljeroth, and J. M. Gottfried, Biphenylene network: A nonbenzenoid carbon allotrope, *Science* **372**, 852 (2021).
- [44] P. Hohenberg and W. Kohn, Inhomogeneous electron gas, *Phys. Rev.* **136**, B864 (1964).
- [45] W. Kohn and L. J. Sham, Self-consistent equations including exchange and correlation effects, *Phys. Rev.* **140**, A1133 (1965).
- [46] J. Soler, E. Artacho, J. Gale, A. Garcia, J. Junquera, P. Ordejon, and D. Sanchez-Portal, The siesta method for *ab initio* order-n materials simulation, *J. Phys.: Condens. Matter* **14**, 2745 (2002).
- [47] J. P. Perdew, K. Burke, and M. Ernzerhof, Generalized Gradient Approximation Made Simple, *Phys. Rev. Lett.* **77**, 3865 (1996).
- [48] N. Troullier and J. L. Martins, Efficient pseudopotentials for plane-wave calculations, *Phys. Rev. B* **43**, 1993 (1991).
- [49] A. Togo, F. Oba, and I. Tanaka, First-principles calculations of the ferroelastic transition between rutile-type and CaCl₂-type SiO₂ at high pressures, *Phys. Rev. B* **78**, 134106 (2008).
- [50] A. Togo and I. Tanaka, First principles phonon calculations in materials science, *Scr. Mater.* **108**, 1 (2015).
- [51] H. T. Stokes, D. M. Hatch, and B. J. Campbell, ISOTROPY software suite.
- [52] H. T. Stokes and D. M. Hatch, FINDSYM: Program for identifying the space-group symmetry of a crystal, *J. Appl. Crystallogr.* **38**, 237 (2005).
- [53] See Supplemental Material at <http://link.aps.org/supplemental/10.1103/PhysRevMaterials.6.016001> for the relaxed atomic positions and optimized lattice vectors for the three studied structures.
- [54] S. Zhang, J. Wang, Z. Li, R. Zhao, L. Tong, Z. Liu, J. Zhang, and Z. Liu, Raman spectra and corresponding strain effects in graphyne and graphdiyne, *J. Phys. Chem. C* **120**, 10605 (2016).
- [55] J. De Sousa, R. Bizardo, V. Sousa Filho, A. Aguiar, V. Coluci, N. Pugno, E. Girao, A. Souza Filho, and D. Galvao, Elastic properties of graphyne-based nanotubes, *Comput. Mater. Sci.* **170**, 109153 (2019).
- [56] U. Khalilov, C. Vets, and E. C. Neyts, Catalyzed growth of encapsulated carbyne, *Carbon* **153**, 1 (2019).
- [57] K. Zhang, Y. Zhang, and L. Shi, A review of linear carbon chains, *Chin. Chem. Lett.* **31**, 1746 (2020).
- [58] P. Ghosez, X. Gonze, and J. P. Michenaud, *Ab initio* phonon dispersion curves and interatomic force constants of barium titanate, *Ferroelectrics* **206-207**, 205 (1998).
- [59] C. Yang, Z. Yu, P. Lu, Y. Liu, H. Ye, and T. Gao, Phonon instability and ideal strength of silicene under tension, *Comput. Mater. Sci.* **95**, 420 (2014).
- [60] F. Liu, P. Ming, and J. Li, *Ab initio* calculation of ideal strength and phonon instability of graphene under tension, *Phys. Rev. B* **76**, 064120 (2007).
- [61] Y. Luo, C. Ren, Y. Xu, J. Yu, S. Wang, and M. Sun, A first principles investigation on the structural, mechanical, electronic, and catalytic properties of biphenylene, *Sci. Rep.* **11**, 19008 (2021).
- [62] F. Ding, K. Bolton, and A. Rosén, Molecular dynamics study of the surface melting of iron clusters, *Eur. Phys. J. D* **34**, 275 (2005).
- [63] S. K. Singh, M. Neek-Amal, and F. M. Peeters, Melting of graphene clusters, *Phys. Rev. B* **87**, 134103 (2013).
- [64] K. Zhang, G. M. Stocks, and J. Zhong, Melting and premelting of carbon nanotubes, *Nanotechnology* **18**, 285703 (2007).
- [65] R. C. Andrew, R. E. Mapasha, A. M. Ukpong, and N. Chetty, Mechanical properties of graphene and boronitrene, *Phys. Rev. B* **85**, 125428 (2012).
- [66] M. Born and H. Huang, *Dynamical Theory of Crystal Lattices* (Oxford University Press, Oxford, 1954).
- [67] Y. Ding and Y. Wang, Density functional theory study of the silicene-like SiX and XSi₃ (X = B, C, N, Al, P) honeycomb lattices: The various buckled structures and versatile electronic properties, *J. Phys. Chem. C* **117**, 18266 (2013).
- [68] J. Drogar, M. Roknabadi, M. Behdani, M. Modarresi, and A. Kari, Hydrogen adsorption on the α -graphyne using *ab initio* calculations, *Superlatt. Microstruct.* **75**, 340 (2014).
- [69] A. Ruiz-Puigdollers and P. Gamallo, DFT study of the role of N- and B-doping on structural, elastic and electronic properties of α -, β - and γ -graphyne, *Carbon* **114**, 301 (2017).
- [70] J. Kang, J. Li, F. Wu, S. S. Li, and J. B. Xia, Elastic, electronic, and optical properties of two-dimensional graphyne sheet, *J. Phys. Chem. C* **115**, 20466 (2011).
- [71] R. Lu, D. Rao, Z. Meng, X. Zhang, G. Xu, Y. Liu, E. Kan, C. Xiao, and K. Deng, Boron-substituted graphyne as a versatile material with high storage capacities of LI and H₂: a multiscale theoretical study, *Phys. Chem. Chem. Phys.* **15**, 16120 (2013).
- [72] D. Xiang, X. Wang, C. Jia, T. Lee, and X. Guo, Molecular-scale electronics: From concept to function, *Chem. Rev.* **116**, 4318 (2016).
- [73] J. Li, Z. Zhang, M. Qiu, C. Yuan, X. Deng, Z. Fan, G. Tang, and B. Liang, High-performance current rectification in a molecular device with doped graphene electrodes, *Carbon* **80**, 575 (2014).
- [74] K. K. Saha, B. K. Nikolic, V. Meunier, W. Lu, and J. Bernholc, Quantum-Interference-Controlled Three-Terminal Molecular Transistors Based on a Single Ring-Shaped Molecule Connected to Graphene Nanoribbon Electrodes, *Phys. Rev. Lett.* **105**, 236803 (2010).
- [75] P. Zhao, Q. H. Wu, H. Y. Liu, D. S. Liu, and G. Chen, A first-principles study of the spin transport properties of a 4H-TAHDI-based multifunctional spintronic device with graphene nanoribbon electrodes, *J. Mater. Chem. C* **2**, 6648 (2014).
- [76] P. V. Silva, A. G. Souza Filho, V. Meunier, and E. C. Girão, Structural and electronic properties of nanotubes constructed from fragmented fullerenes, *Carbon* **147**, 616 (2019).
- [77] Y. Min, J. Fang, C. Zhong, Z. Dong, C. Wang, T. Xue, and K. Yao, Contact transparency inducing negative differential resistance in nanotube-molecule-nanotube junction predicted by first-principles study, *Phys. Lett. A* **378**, 1170 (2014).
- [78] R. Rahighi, O. Akhavan, A. S. Zeraati, and S. M. Sattari-Esfahlan, All-carbon negative differential resistance nanodevice using a single flake of nanoporous graphene, *ACS Appl. Electron. Mater.* **3**, 3418 (2021).

- [79] A. Mohammadi and E. Zaminpayma, Armchair α -graphyne nanoribbons as negative differential resistance devices: Induced by nitrogen doping, *Organic Electron.* **61**, 334 (2018).
- [80] C. Xu, P. Ning, C. Luo, L. Cao, X. Deng, and G. Zhou, Electronic properties and spintronic applications of r-N-graphyne nanoribbons, *J. Phys. E* **136**, 115003 (2022).
- [81] J.-J. Zheng, X. Zhao, S. B. Zhang, and X. Gao, Tight-binding description of graphyne and its two-dimensional derivatives, *J. Chem. Phys.* **138**, 244708 (2013).
- [82] H. Jafarzadeh and M. Ghodrati, Investigation of electronic and optical properties of zigzag-graphyne nanotubes by using a tight-binding method, *J. Electron. Mater.* **48**, 4669 (2019).